Multi-objective optimization of PCM-fin structure for staggered Li-ion battery packs

Chenghui QIU, Chongtian WU, Xiaolu YUAN, Linxu WU, Jiaming YANG, and Hong SHI[ID]*

College of Energy & Power Engineering, Jiangsu University of Science and Technology, Zhenjiang, Jiangsu, 212003, P.R. China

Abstract. Endurance capability is a key indicator to evaluate the performance of electric vehicles. Improving the energy density of battery packs in a limited space while ensuring the safety of the vehicle is one of the currently used technological solutions. Accordingly, a small space and high energy density battery arrangement scheme is proposed in this paper. The comprehensive performance of two battery packs based on the same volume and different space arrangements is compared. Further, based on the same thermal management system (PCM-fin system), the thermal performance of staggered battery packs with high energy density is numerically simulated with different fin structures, and the optimal fin structure parameters for staggered battery packs at a 3C discharge rate are determined using the entropy weight-TOPSIS method. The result reveals that increasing the contact thickness between the fin and the battery (X) can reduce the maximum temperature, but weaken temperature homogeneity. Moreover, the change of fin width (A) has no significant effect on the heat dissipation performance of the battery pack. Entropy weight-TOPSIS method objectively assigns weights to both maximum temperature (T_{max}) and temperature difference (ΔT) and determines the optimal solution for the cooling system fin parameters. It is found that when $X = 0.67$ mm, $A = 0.6$ mm, the staggered battery pack holds the best comprehensive performance.

Key words: staggered arrangement, phase change material, fin, entropy weight-TOPSIS, multi-objective optimization, thermal management.

1. INTRODUCTION

Electric vehicles are expected to become the preferred mode of transportation in the future because of their energy saving and environmental protection advantages as compared to fuel vehicles [1]. Due to their high energy and power density, lithium-ion batteries are widely regarded as the ideal choice for electric vehicle power sources [2]. However, with the increasing demand for higher battery power density and faster charging rates, electric vehicle batteries generate more heat and thus temperature control becomes a technical challenge [3]. The optimal operating temperature range for lithium-ion batteries is 20–50°C, with the divergence in maximum temperature between cells controlled within 5°C [4]. Improper thermal management controls will accelerate the decay of battery capacity and life under certain working conditions, even causing safety accidents such as explosions [5–8]. Therefore, considering the need for continuous improvement in safety performance and energy density of electric vehicles, it is crucial to propose an efficient battery thermal management system that can meet the necessary conditions.

Many studies have been conducted on battery thermal management technologies, which include air cooling [9,10], liquid cooling [11,12], heat pipe cooling [13,14], phase change material cooling [15,16] and hybrid cooling [17,18]. Among these cooling strategies, PCM is studied extensively by researchers due to its advantages of high latent heat, low cost, and thermal stability [19]. Furthermore, phase change material cooling has significant advantages over active systems such as air cooling and liquid cooling, including its simpler structure and no additional energy consumption. Nevertheless, pure PCM has poor thermal conductivity, which limits the application and advancement of PCM-based battery thermal management technology because it lowers the transfer rate of heat during continuous cycle charging and increases the risk of battery thermal runaway [20]. Therefore, increasing the heat conduction of PCM has been the main focus of numerous studies in recent years. For example, thermal conductivity enhancers such as expanded graphite and metal foam are added to PCM to synthetize CPCMS with a relatively high heat conductivity coefficient. Huang *et al.* investigated the thermophysical properties of pure paraffin, expanded graphite and paraffin CPCM. They found that expanded graphite and paraffin composite phase change materials with 94% porosity provide the best thermal management properties [21]. Zhang *et al.* proposed a new composite phase change material based on aluminum nitride, using expanded graphite and aluminum nitride as thermal conductivity enhancers. They demonstrated that the CPCM shows improved thermal conductivity, high mechanical strength and excellent insulation properties when 20% aluminum nitride powder is added [22].

However, it is found that the particle settling phenomenon is an unavoidable problem for composite phase change materials during the actual cyclic charging and discharging process [23]. Therefore, fins, which can enhance the heat exchange surface and decrease thermal resistance, become a more preferable option for dissipating heat from the battery. Fan *et al.* discovered that the PCM-fins system increases the operating time by 98.4%

Bull. Pol. Acad. Sci. Tech. Sci., vol. 71, no. 4, p. e145677, 2023

1

as compared to the pure PCM cooling system through a simulation combined with experimental research method. Besides, the performance of the battery thermal management system is significantly enhanced by optimizing the length and distribution of the fin [24]. Verma *et al.* designed a novel BTMS that consists of PCM and rectangular longitudinal fins in a high temperature environment. They discovered that increasing the thickness of PCM and the length of fins can improve the minimum liquid fraction by 91.7%, and that adding fins improves the battery pack temperature uniformity significantly [25]. Ambekar *et al.* investigated five fin structures to optimize the thermal performance of the battery module based on the actual heat generation of the battery. Taking into account the system heat dissipation rate and the effective utilization rate of the PCM, it was determined that the FS-3 fin structure is most effective in keeping the maximum temperature of the battery module below 60°C after 2.5 charge/discharge cycles with 2C and 3C discharge rates, respectively [26]. Qi *et al.* used response surface analysis to determine the optimal fin height, width and spacing for a cylinder-shaped lithium-ion battery with a rated capacity of 18650 mAh. Results indicated that fin height is more important than other factors in affecting the temperature spike of the battery and the liquid phase fraction of the PCM [27]. Mansir *et al.* simulated the thermal dissipation of fins using a two-dimensional view of triangular shape, and numerically analyzed the effect of fin arrangement and width. They found that extending the width of the fins arranged as F1 and F2 from 1 cm to 4 cm reduces peak temperature by 2.04°C and 2.15°C, and enhances the heat transfer coefficients by 20% and 19.4%, respectively, which also improves the PCM liquid phase fraction [28]. Akula *et al.* proposed a fin-eicosane (EI) – expanded graphite (EG) CPCM. It is found that the composite heat sink system with 260 fins coupled with 70% eicosane and 30% expanded graphite performs the best thermally, when compared with 130 fins and 260 fins with different weight fractions of phase change material [29].

In conclusion, the majority of studies on enhancing PCM thermal conductivity with fins concentrate on modifying the shape of the fin. Few studies have focused on the coupling multi-objective problems of thermal performance and energy density in battery pack configurations. However, as endurance requirements in the field of electric vehicles increase, increasing the energy density of energy storage devices in a limited space also becomes worth further investigation under the premise of ensuring safety and reliability. Therefore, in order to solve the design problem of higher energy density in the limited space of battery packs, this paper proposes an innovative battery cooling system applied to the staggered battery pack with a PCM-fins cooling system. Based on this, a response surface model is constructed to fit the link between the parameters of the fin structure and the battery thermal performance index. The entropy weight-TOPSIS method is introduced to comprehensively analyze the weights of the temperature spike and temperature homogeneity to obtain the optimal fin structure parameters, which solves the technical bottleneck of ensuring heat dissipation while maintaining a high energy density of the battery at the same volume.

2. PHYSICAL MODEL DESCRIPTION AND MATHEMATICAL FORMULATION

2.1. Physical model

The physical model comprises 17 model 26650 (26 mm in diameter and 65 mm in height) Li-ion cylindrical cells, PCM, fins and an aluminum container, as shown in Fig. 1. 17 lithium-ion cells are arranged in staggered lines, with the aluminum container filled with paraffin in between the surrounding of each battery, and the fins attached to the surface of the batteries. As depicted in Fig. 2, the spacing between the batteries is 36 mm, the thickness and the overall height of the phase change material is 5 mm and 75 mm, respectively. The structure of the fins is shown in Fig. 3, and due to the size restriction of the aluminum shell, the total transverse length of a single fin is fixed at 10 mm, meaning that $X + Y = 5$ mm, and the height of the fin is equal to that of the battery, which is 65 mm. In addition, the fin material used in the model is aluminum. Herein, the contact thickness between the fin and the battery X (mm) and fin width A (mm) are optimized for optimal performance. The specific thermophysical properties of battery, paraffin, air and fin are shown in Table 1 [30, 31], and the technical specifications of the battery cell are listed in Table 2.

Table 1
Specific thermophysical properties of battery, paraffin, air and fin

Thermophysical properties	Battery	Paraffin (Rubitherm RT28 HC)	Air	Fin
Density /kg·m^{-3}	2962.4	880	1.225	2719
Thermal conductivity /W·(m·K)$^{-1}$	30	0.2	0.0242	202.4
Heat capacity /J·(kg·K)$^{-1}$	970	2800	1006.43	871
Dynamic viscosity / kg·(m·s)$^{-1}$	–	0.02	1.7894e–05	–
Melting heat /J·kg^{-1}	–	245000	–	–
Phase change temperature /°C	–	27~28	–	–
Discharge rate	2C/3C/4C	–	–	–
Heat generation rate /W·m^{-3}	99104/222984/ 371640	–	–	–

2

Bull. Pol. Acad. Sci. Tech. Sci., vol. 71, no. 4, p. e145677, 2023

Multi-objective optimization of PCM-fin structure for staggered Li-ion battery packs
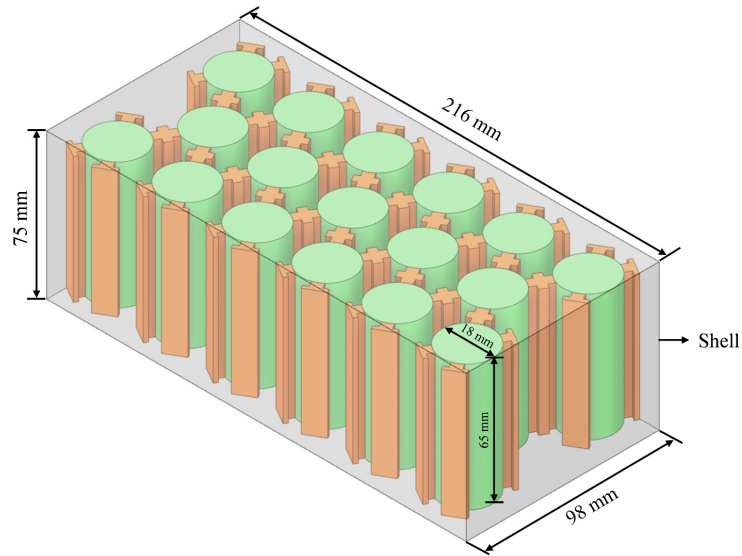

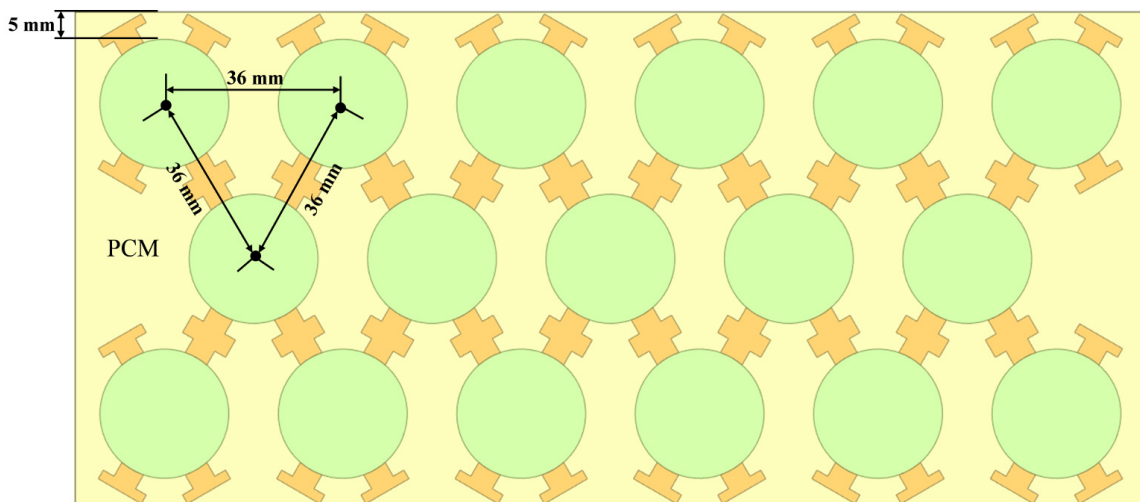**Fig. 1.** Schematic diagram of the staggered battery pack

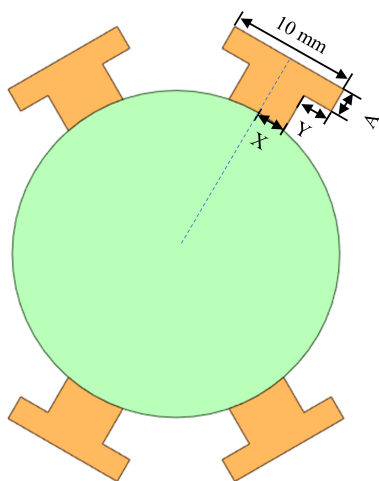**Fig. 2.** Schematic diagram of the structural arrangement for staggered battery pack (top view)

Fig. 3. Schematic diagram of the fin structure

Table 2
Technical specifications of battery cell

Specifications	Parameters
Nominal voltage /V	3.6
Nominal capacity /Ah	3.2
Internal resistance /mΩ	40
Charge-discharge cutoff voltage /V	4.2/2.5
Anode material	$LiCoO_2$
Cathode material	Graphite
Electrolyte material	LiPF6

Bull. Pol. Acad. Sci. Tech. Sci., vol. 71, no. 4, p. e145677, 2023

3

C. Qiu, C. Wu, X. Yuan, L. Wu, J. Yang, and H. Shi

2.2. Mathematical formulation

2.2.1. Battery model

An important feature of a lithium-ion battery operation is heat generation. Due to the intricate electrochemical reactions taking place throughout the charging and discharging cycle, a significant quantity of heat is produced, which affects the performance of lithium-ion batteries in many ways. Several heat generation models have been built to comprehensively analyze the heat generation and heat transmission mechanisms of lithium-ion batteries. In this paper, the heat generation estimation of the 26650 Li-ion battery is based on Bernardi's theoretical formulation [32], as follows:

$$q_V = \frac{I}{V_b}\left[(E_0 - E) \pm T\frac{\partial E_0}{\partial T}\right] = \frac{1}{V_b}\left(I^2 R_b \pm IT\frac{\partial E_0}{\partial T}\right), \quad (1)$$

where: q_V is the heat generation rate of the battery, W; V_b is the volume of the battery, m^{-3}; I is the charge/discharge current, A; E_0 and E are the open-circuit and terminal voltages of the battery, respectively, V; R_b is battery internal resistance, Ω; T is the ambient temperature to which the battery is exposed, K; $\partial E_0/\partial T$ is the heat entropy coefficient of the battery.

For the mathematical description of the thermal conductivity phenomenon of lithium-ion batteries, this study regards it as a solid three-dimensional transient thermal conductivity problem with an internal heat source based on the energy balance equation in the simulation study. The mathematical model is defined by equation (2):

$$\rho C_p \frac{\partial T}{\partial \tau} = \frac{\partial}{\partial x}\left(\lambda_x\frac{\partial T}{\partial x}\right) + \frac{\partial}{\partial y}\left(\lambda_y\frac{\partial T}{\partial y}\right) + \frac{\partial}{\partial z}\left(\lambda_z\frac{\partial T}{\partial z}\right) + q_V, \quad (2)$$

where: ρ represents density of the battery, kg/m^3; C_p is the heat capacity of the battery, J·(kg·K)$^{-1}$; T represents temperature of the battery, K; τ is time, s; while λ_x, λ_y and λ_z stand for the thermal conductivity of the x, y and z direction of the battery, respectively.

2.2.2. PCM model

In this paper, the complex phase transition process of PCM is modelled based on the enthalpy change method [33, 34], and the following assumptions are made before the numerical study to simplify the model:

1. Thermophysical properties of PCM that are uniform and constant, such as density and thermal conductivity, are studied;
2. The liquid phase of PCM is incompressible;
3. Contact thermal resistance between PCM and battery is negligible.

Based on the above assumptions, the control equations based on continuity equation, momentum equation and energy equation are shown below:

1. Continuity equation:

$$\frac{\partial \rho_{\text{PCM}}}{\partial \tau} + \frac{\partial(\rho_{\text{PCM}}u_j)}{\partial x_j} = 0. \quad (3)$$

2. Momentum equation:

$$\frac{\partial(\rho_{\text{PCM}}u_j)}{\partial \tau} + \frac{\partial(\rho_{\text{PCM}}u_i u_j)}{\partial x_j} = -\frac{\partial P}{\partial x_i}$$
$$+ \frac{\partial}{\partial x_i}\left(\mu\frac{\partial u_i}{\partial x_j}\right) + \rho_{\text{PCM}}g + S, \quad (4)$$

where: S denotes momentum source term, which is defined as:

$$S = \frac{(1-\beta)^2}{\beta^3 + \omega}A_{\text{mush}}u_j, \quad (5)$$

$$\beta = \begin{cases} 0, & T < T_s \\ \dfrac{T - T_s}{T_l - T_s}, & T_s < T < T_l, \\ 1, & T > T_l, \end{cases} \quad (6)$$

where: β represents the liquid fraction, %; the constant ω is in the vicinity of 10^{-3}, which is a small number; A_{mush} is the mushy zone constant, which is set to 10^5 kg·(m^2·s)$^{-1}$ in the fluent setup; T_s and T_l represent the paraffin solidus and liquidus temperatures, which are 300.15 K and 301.15 K, respectively, in this paper.

3. Energy equation:

$$\frac{\partial(\rho_{\text{PCM}}H)}{\partial t} + \nabla \cdot (\rho_{\text{PCM}}\vec{u}H) = \nabla(k_{\text{PCM}}\nabla T), \quad (7)$$

where: ρ_{PCM} is the density of PCM, kg·m^{-3}; $\vec{u}$ is the speed of PCM, m·s^{-1}; k_{PCM} is thermal conductivity, W·(m·K)$^{-1}$; and H is total enthalpy, which can be calculated as follows:

$$H = h + \Delta H, \quad (8)$$

$$h = h_{\text{ref}} + \int_{T_{\text{ref}}}^{T} C_p \, dT, \quad (9)$$

$$\Delta H = \beta\gamma, \quad (10)$$

where: h and h_{ref} denote sensible heat and reference enthalpy, respectively, kJ·kg^{-1}; γ is the specific latent heat of PCM, kJ·kg^{-1}; and T_{ref} is the ambient temperature, K.

2.3. Initial and boundary conditions

In this paper, the following boundary conditions are employed to solve the control equations in ANSYS FLUENT. The pressure-velocity coupling problem is numerically calculated using the SIMPLE algorithm, with the step size set to 1 s, and the number of iterations per step set to 20. The simulation in this research includes three different discharge rates (2C, 3C, and 4C). And the initial state of the model is as follows:

$$T_{\text{battery}}(x,y,z) = T_{\text{PCM}}(x,y,z) = T_{\text{amb}}, \quad (11)$$

where: T_{amb} is ambient temperature and is taken as 298.15 K in this paper.

Boundary conditions between PCM and the battery:

$$k_{\text{battery}} \frac{\partial T_{\text{battery}}}{\partial n} = k_{\text{PCM}} \frac{\partial T_{\text{PCM}}}{\partial n}, \qquad (12)$$

where: k_{battery} denotes thermal conductivity, $\text{W}\cdot(\text{m}\cdot\text{K})^{-1}$; and T_{battery} is the temperature of the battery, K.

The boundary conditions between PCM and the aluminum enclosure can be described as:

$$k_{\text{PCM}} \frac{\partial T_{\text{PCM}}}{\partial n} = h (T_{\text{PCM}} - T_{\text{amb}}), \qquad (13)$$

where: k_{PCM} represents thermal conductivity of PCM, $\text{W}\cdot(\text{m}\cdot\text{K})^{-1}$; h is the heat transfer coefficient for air convection. Considering that the battery is in a natural convection state in this paper, taking 5 $\text{W}\cdot(\text{m}^2\cdot\text{K})^{-1}$.

3. NUMERICAL SIMULATION METHODOLOGY

3.1. Validation of numerical approach

To ensure the model's reliability, it is necessary to conduct validation tests. Thus the experimental system depicted in Fig. 4 was constructed. Figure 5 illustrates a schematic diagram of the BTMS, which consists of an 18650 Li-ion battery, phase change material and a container. The phase change material used is paraffin with a phase transition temperature of 30°C. Table 3 provides details on these thermophysical characteristics. During the experiment, the cooling system was placed in a thermostat incubator set at 20°C with natural convection heat transfer. The 0.5 mm K-type thermocouples with 1 s response time and ±1.0°C accuracy were used to monitor BTMS temperatures.

Figure 6 displays the specific positions of three thermocouples. Additionally, the average value of 3 points is taken as the index for evaluating the thermal performance of BTMS.
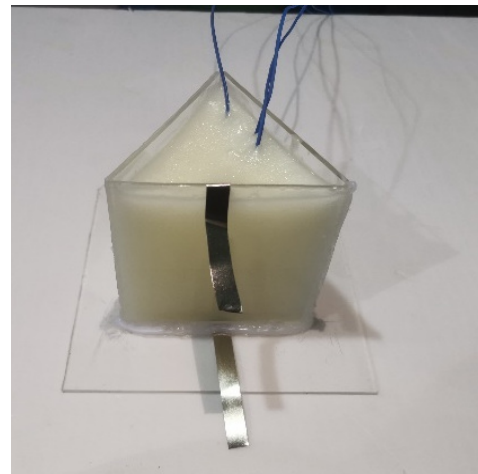

Fig. 5. Schematic diagram of BTMS

A comparison of the simulated and experimental results is shown in Fig. 7, where it can be found that the temperature curve of the experiment is mostly in agreement with that of the simulation, with the maximum relative error rate occurring at 1200 s, which is 2.09%. Between 1000 s and 1200 s, the simulated temperature is higher than the experimental temperature, which is mainly because of the enhanced convective heat exchange between PCM and the environment at the top of the container after PCM started to melt in the experiment.
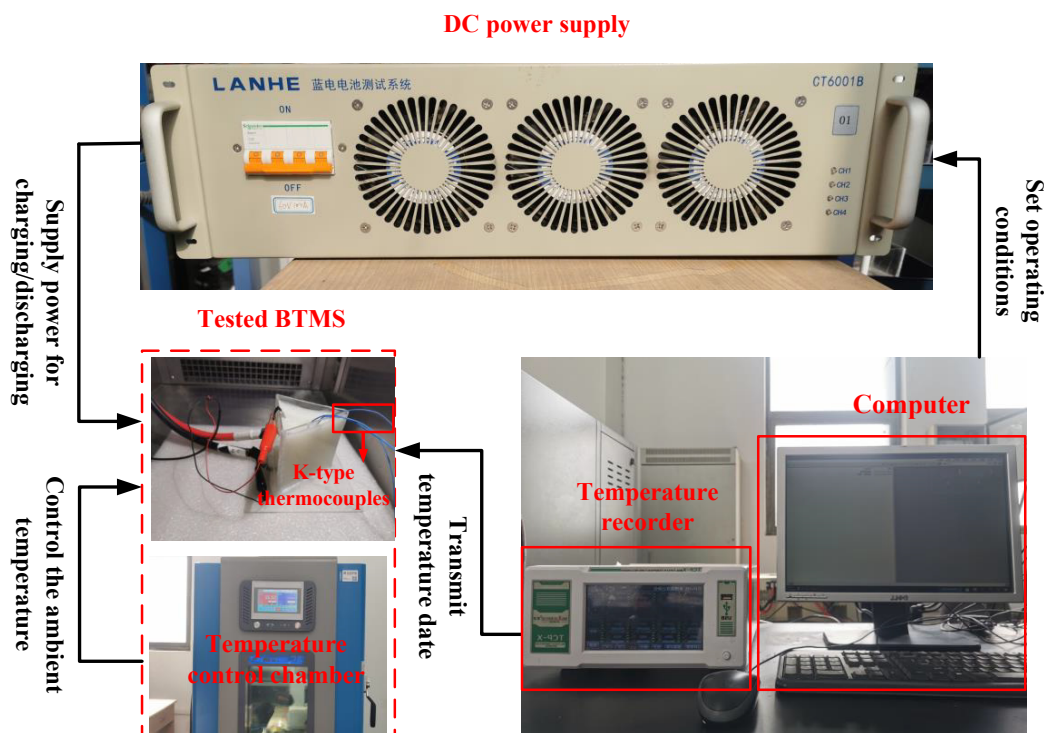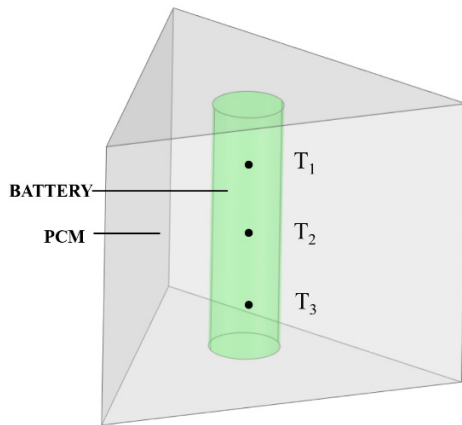

Fig. 4. Experimental system

Bull. Pol. Acad. Sci. Tech. Sci., vol. 71, no. 4, p. e145677, 2023

5

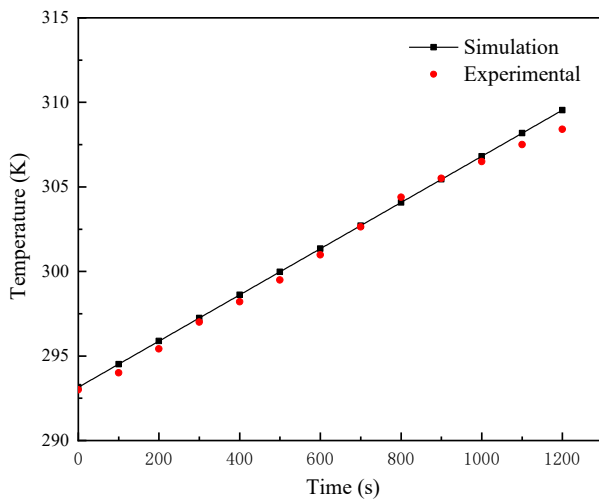**Fig. 6.** Sketch of thermocouples' locations in battery

Fig. 7. Comparison of simulated and experimental results at 3C discharge rate

Table 3
Specific thermophysical properties of battery and paraffin

Thermophysical properties	Battery	Paraffin
Density /kg·m^{-3}	2684.30	730
Thermal conductivity /W·(m·K)$^{-1}$	30	0.21
Heat capacity /J·(kg·K)$^{-1}$	1282	2000
Dynamic viscosity /kg·(m·s)$^{-1}$	–	300
Melting heat /J·kg^{-1}	–	220000
Phase change temperature /K	–	303.15∼304.15
Discharge rate	3C	–
Heat generation rate /W·m^{-3}	52090	–

3.2. Grid independence

In this paper, tetrahedral mesh is generated using ICEM software, as shown in Fig. 8. To ensure accuracy of the numerical results, five different sizes of grids are selected for a rigorous grid independence test, in which the maximum battery temperature (T_{max}) at 3C discharge rate is used as the standard of the test. Numerical results for the five cases are listed in Table 4.
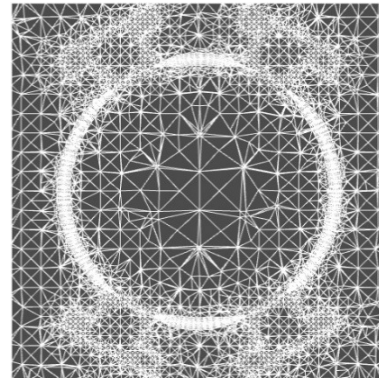

Fig. 8. Schematic diagram of tetrahedral mesh for a single battery

Table 4
Numerical results under different sizes of grids

Case	Numbers of the grid elements	T_{max}
I	9 108 974	312.45
II	15 371 484	313.18
III	23 411 318	313.44
IV	29 710 325	313.46
V	34 601 376	313.47

As can be seen from Table 4, the maximum temperature change is only 0.03 K when the cell number increases from 23 411 318 to 34 601 376, indicating that 23 411 318 cells is a large enough number for this research. Considering the calculation efficiency and the accuracy of the numerical simulation results, the grid number of 23 411 318 is finally selected for calculation in this paper.

4. THERMAL CHARACTERISTICS OF STAGGERED BATTERY PACK

In this paper, the contact thickness between the fin and the battery X (range from 0.5 mm to 4.5 mm) and fin width A (range from 0.5 mm to 2.5 mm) are used as variation parameters, and the maximum battery temperature (T_{max}) and the temperature difference (ΔT) are selected as the evaluation indices for the thermal performance of BTMS. To ensure accuracy of the simulation results, three temperature measurement points are distributed along the axial direction of the battery in this study, as shown in Fig. 9. Additionally, Fig. 9 illustrates the results of temperature values for various temperature measurement points within the battery pack. It is evident from the curves that the internal temperature distribution of the battery shows a trend of high in the middle and low at both poles. In detail, the temperature difference between the upper and lower poles is negligible, and the temperature at the middle point is higher than

6

Bull. Pol. Acad. Sci. Tech. Sci., vol. 71, no. 4, p. e145677, 2023

the temperature at both poles, with a maximum difference of 0.4 K. Therefore, the center point of the battery is selected as the maximum battery temperature (T_{max}) measurement point in this paper.
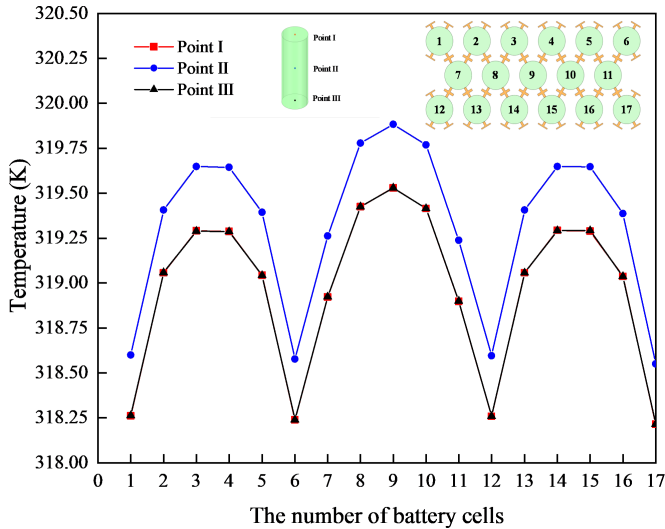

Fig. 9. Temperature values of different temperature measurement points in the battery pack

4.1. Comparison between aligned and staggered battery packs on thermal characteristics

In the practical application of the battery pack, for the same total volume, the staggered pack possesses higher energy density than the batteries with aligned arrangement. Therefore, to evaluate the thermal efficiency of two different configurations, the thermal characteristics of two battery packs with 3C discharge rate are investigated in this section.

Fig. 10 and Fig. 11 illustrate the schematic diagram of the structural arrangement for aligned and staggered battery packs, respectively.
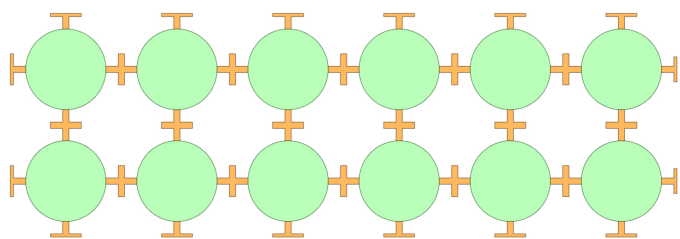

Fig. 10. Schematic diagram of structural arrangement for aligned battery pack

Table 5 shows the thermal performance of the two battery packs at the end of discharge. As shown in Table 5, T_{max} of both aligned and staggered battery packs are 312.37 K, and 312.62 K, respectively, at a 3C discharge rate. Additionally, Fig. 12 and Fig. 13 show the temperature contours of the middle cross section within the battery pack in the aligned and staggered arrangements, respectively. It can be seen from the
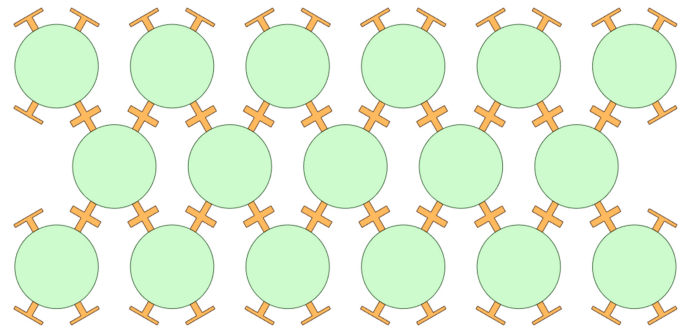

Fig. 11. Schematic diagram of structural arrangement for staggered battery pack

Table 5
Thermal performance of the two battery packs at the end of discharge

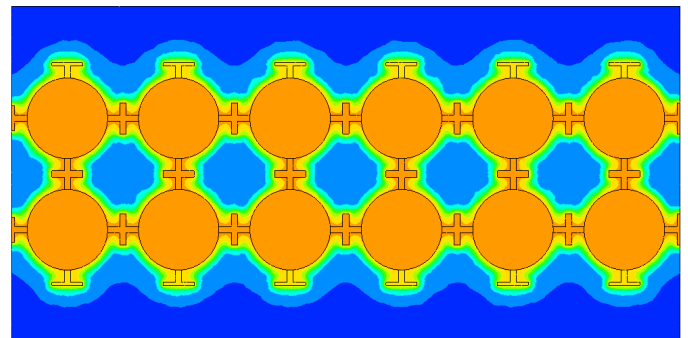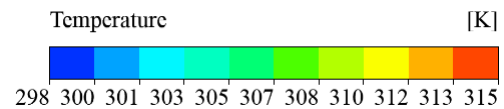| Arrangements	T_{max} [K]	ΔT [K]
aligned	312.37 K	0.06 K
staggered	312.62 K	1.45 K

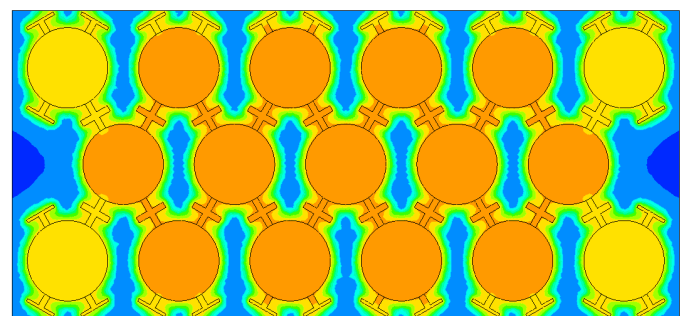**Fig. 12.** Temperature contour of the battery module with aligned arrangement

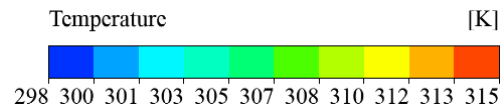**Fig. 13.** Temperature contour of the battery module with staggered arrangement

Bull. Pol. Acad. Sci. Tech. Sci., vol. 71, no. 4, p. e145677, 2023

7

C. Qiu, C. Wu, X. Yuan, L. Wu, J. Yang, and H. Shi

contours that the ΔT of the battery pack with staggered arrangement is higher than that of aligned arrangement obviously, which is 1.45 K and 0.06 K, respectively. Although T_{max} and ΔT of the latter (staggered arrangement) are higher than those of the former (aligned arrangement), the divergence between the T_{max} of the two packs at the end of discharge is slight, only 0.25 K. Furthermore, ΔT of the staggered battery pack is 1.45 K, which is within the standard temperature difference range of 5°C [4]. Accordingly, taking into account the thermal performance and energy density of the battery pack, the battery pack with staggered arrangement is chosen for further study.

4.2. Effect of fin thickness-X on thermal characteristics

As is well known, fin structure significantly affects the efficiency of heat dissipation in BTMS. For this purpose, heat dissipation characteristics of staggered battery packs with various thicknesses X (range from 0.5 mm to 4.5 mm) at 2C, 3C and 4C discharge rates are considered in this section. Figure 14 and Fig. 15 describe the distribution of T_{max} and ΔT of battery packs with different fin thicknesses X at various discharge rates.
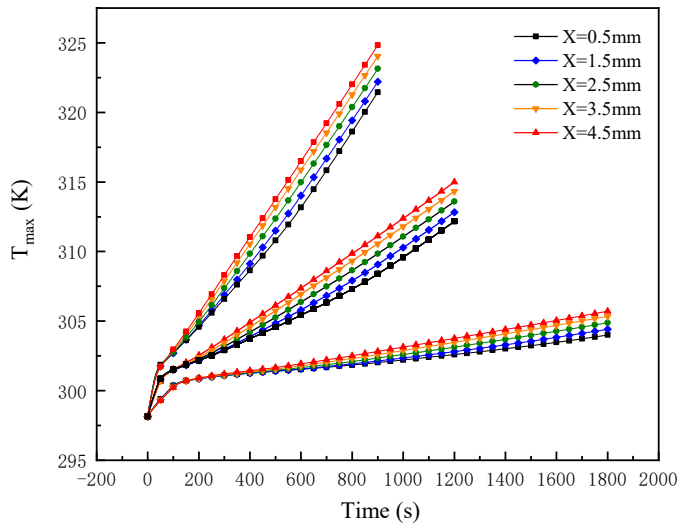

Fig. 15. Variations of ΔT under different X at different discharge rates

Fig. 14. Variations of T_{max} under different X with time at different discharge rates
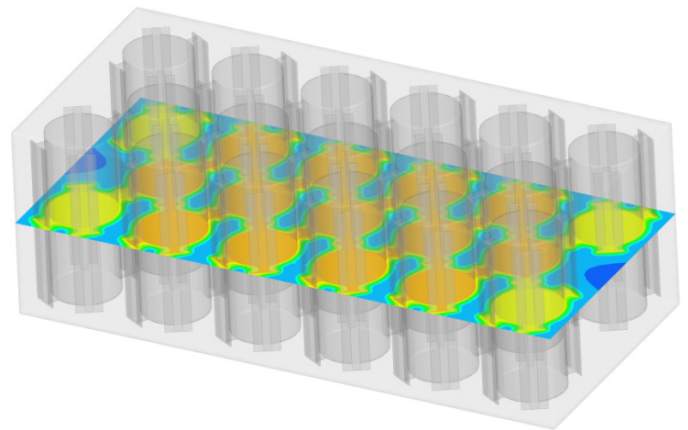
Fig. 16. Schematic diagram of the location of the middle cross section within battery pack

As shown in Fig. 14 and Fig. 15, when fin thickness X is increased from 0.5 mm to 4.5 mm, T_{max} increases by 1.71 K, 2.83 K and 3.39 K at 2C, 3C and 4C discharge rates respectively. Accordingly, ΔT decreases by 0.06 K, 0.42 K and 0.72 K, respectively. This indicates that the maximum temperature of the battery pack increases with X, while temperature uniformity also improves with the increase of X. To elaborate on BTMS's thermal characteristics, the temperature distributions of the middle cross section within battery packs at the end of discharge are presented as the basis for analysis. Specific location of the middle cross section is illustrated in Fig. 16. Meanwhile, Fig. 17 depicts the temperature distributions at different fin thicknesses.

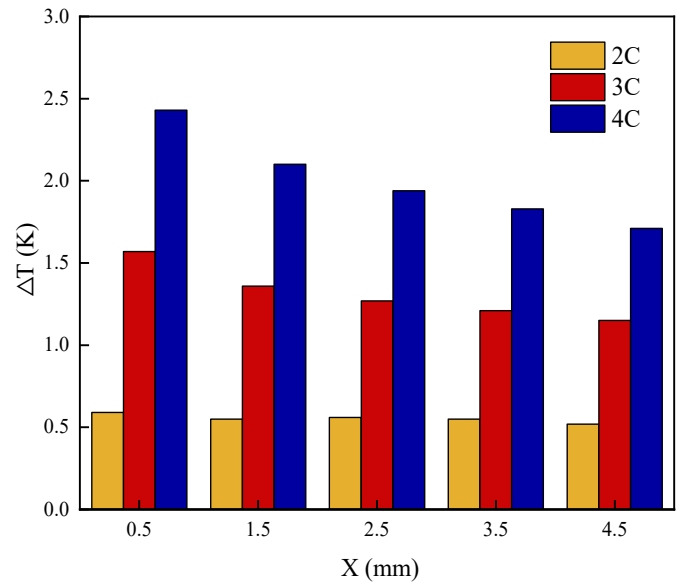As can be seen from Fig. 17, with the increase of X, the heat transfer area between the battery and the fins increases. Due to the high thermal conductivity of fins, the heat generated by the battery is transferred to the fins through a larger heat transfer surface, and is absorbed by PCM around the fins, which improves temperature uniformity between the batteries. However, the increase in the thickness of the fins in a limited volume will inevitably result in a decrease in the volume of PCM. And there is an overall decreasing trend of the heat transfer area between PCM and fin as X increases, which can be clearly seen from Fig. 17. Although thicker fins can rapidly transfer the heat generated in the battery to the fins, it cannot be absorbed by sufficient latent heat of PCM due to the reduction of PCM volume and contact area between PCM and the fins. Therefore, during the discharge process, the increase of X can only enhance heat transfer capability from batteries to the fins, which contributes to improving temperature homogeneity. Meanwhile, the temperature spike of the battery pack is poorly controlled when X increases from 0.5 mm to 4.5 mm, which is mainly because of the decrease of effective utilization of PCM.
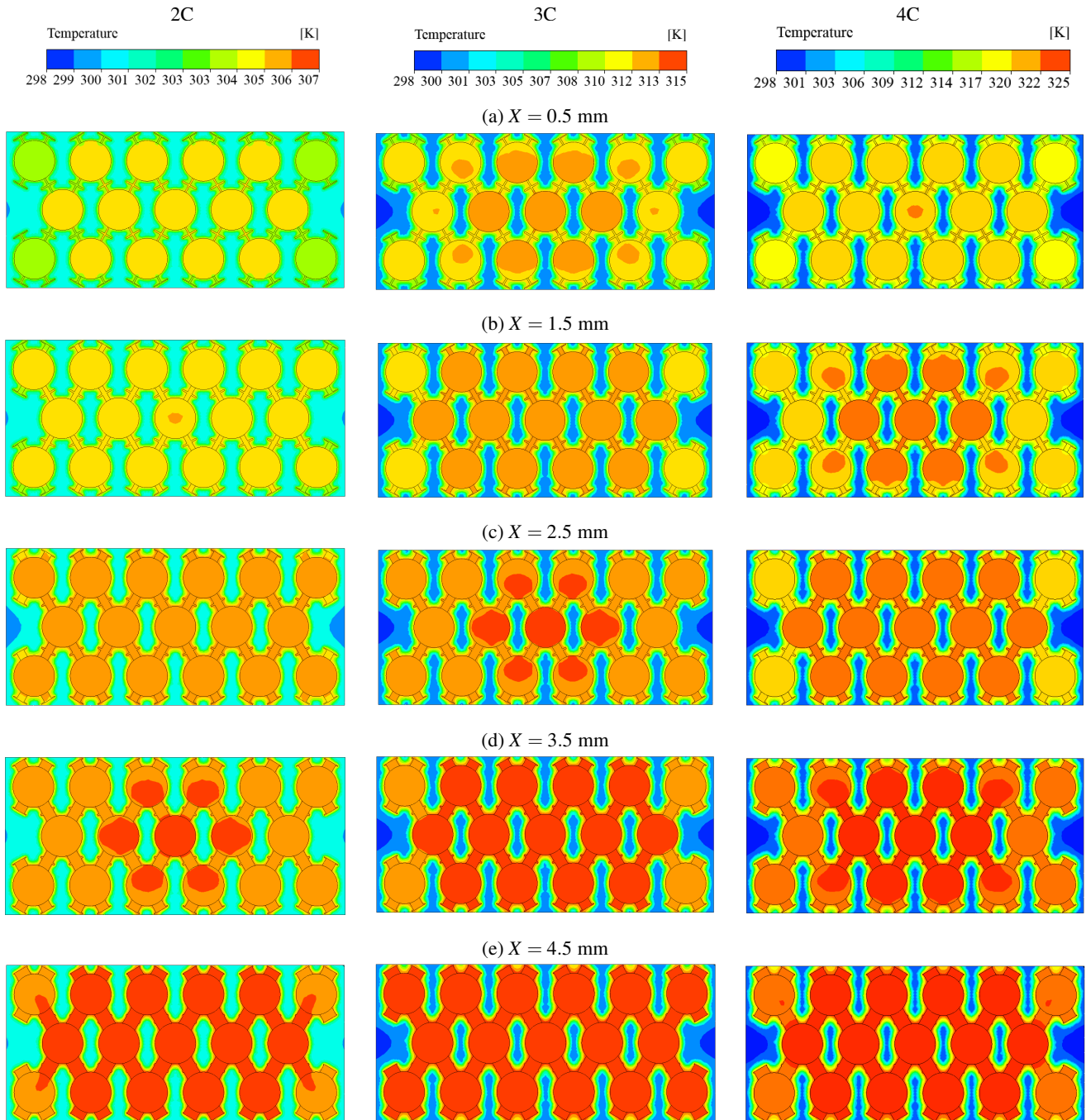
Fig. 17. Temperature contours of battery packs with different X at three discharge rates

4.3. Effect of fin width *A* on thermal characteristics

Fin width (A) is another factor considered in this section to investigate the thermal characteristics of a staggered battery pack. Fig. 18 and Fig. 19 display the variation curves of T_{max} and the ΔT under different fin widths A (range from 0.5 mm to 2.5 mm) at various discharge rates.

As shown in Fig. 18 and Fig. 19, as for battery packs with various widths of fins, the curves of T_{max} with time are very similar, which copies the same rules that apply to different discharge rates. When the fin width (A) increases from 0.5 mm to 2.5 mm, T_{max} increases by 0.55 K, 0.97 K and 1.13 K for 2C,

3C and 4C discharge rates, respectively. Accordingly, ΔT increases by 0.11 K, 0.08 K and 0.08 K, respectively. From the change mentioned above, it can be observed that the change during the discharge process is distinctly small, which indicates that the change of A has little influence on the thermal performance of the battery pack. Figure 20 demonstrates the temperature distributions of the middle cross section within the battery packs with various fin widths.

As depicted in Fig. 20, when A increases from 0.5 mm to 2.5 mm, the heat transfer areas between PCM and fins change less. However, in a fixed-size aluminum container, the increase
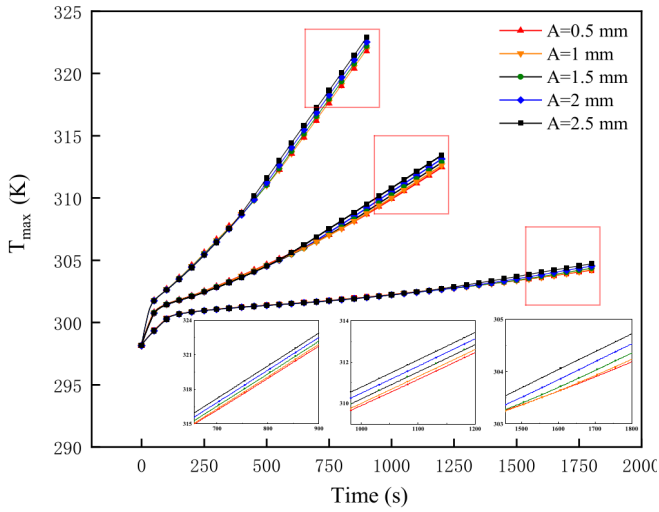
Bull. Pol. Acad. Sci. Tech. Sci., vol. 71, no. 4, p. e145677, 2023

9

C. Qiu, C. Wu, X. Yuan, L. Wu, J. Yang, and H. Shi

Fig. 18. Variations of T_{max} under different A with time at different discharge rates
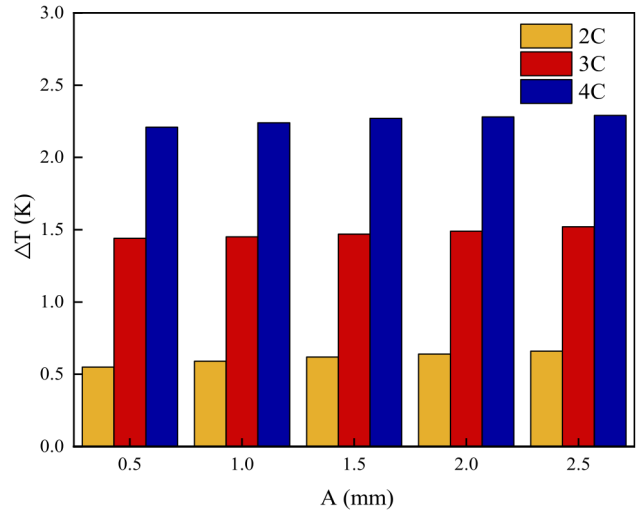
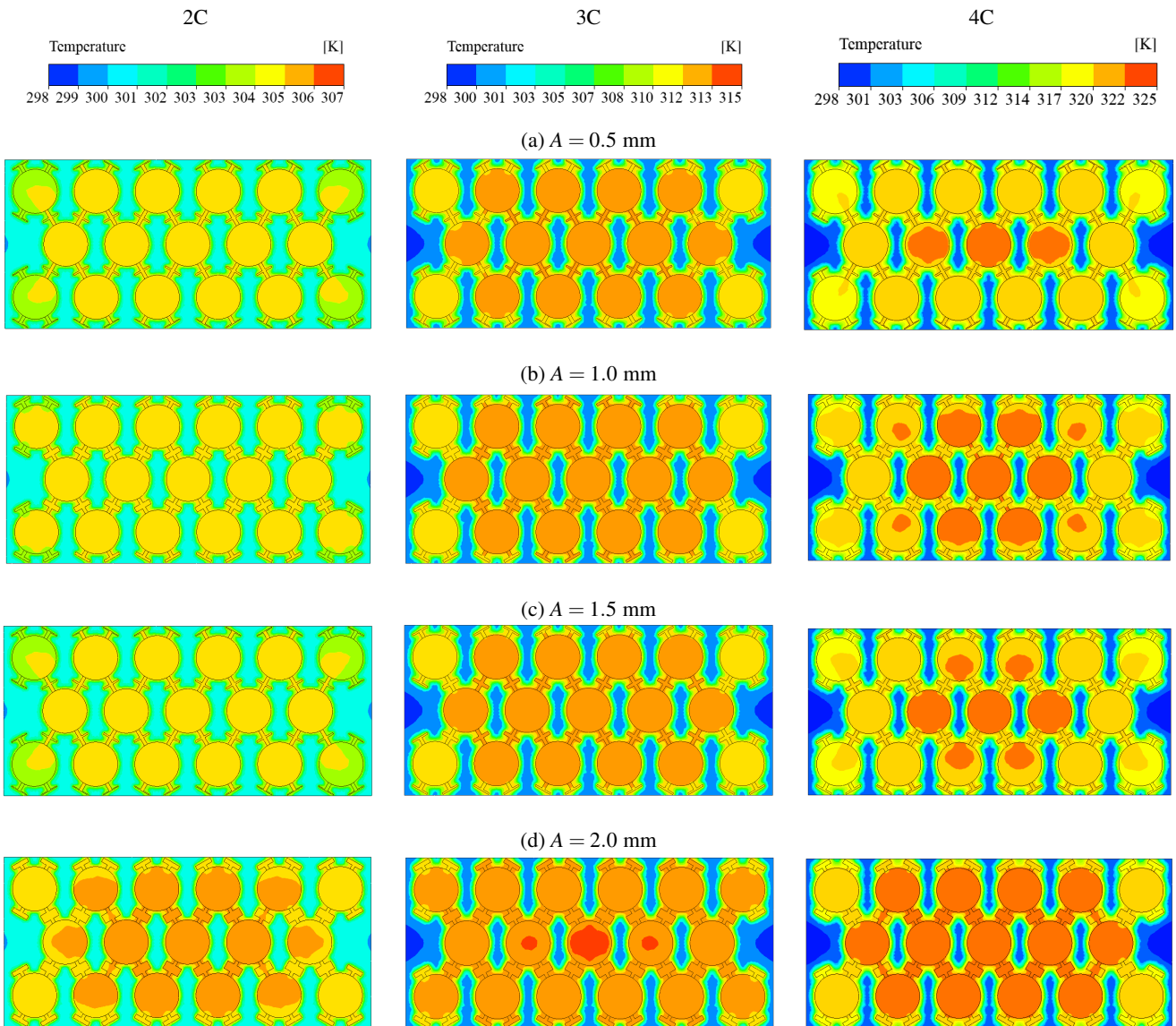**Fig. 19.** Variations of ΔT under different A at different discharge rates

Fig. 20. (a)–(d)

10

Bull. Pol. Acad. Sci. Tech. Sci., vol. 71, no. 4, p. e145677, 2023
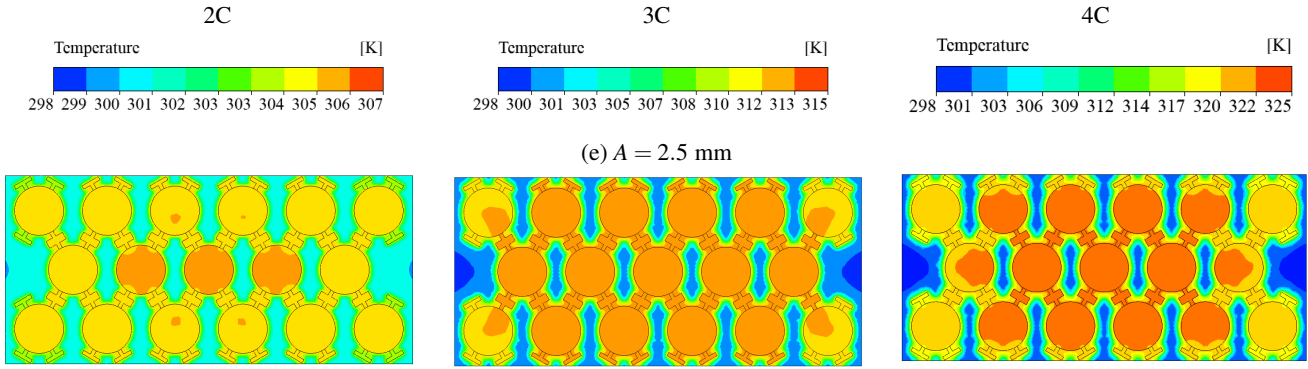
(e) $A = 2.5$ mm

Fig. 20. Temperature contours of battery packs with different A at three discharge rates

of A reduces PCM's volume, at which the heat dissipation efficiency of fins exceeds the heat absorption efficiency of PCM, thus the heat generated by the battery cannot be dissipated effectively. Therefore, increasing the fin widths not only fails to enhance the battery module's thermal performance, but also increases the weight of the battery module. Based on the above analysis, the battery module holds the best thermal performance when A is 0.5 mm.

5. OPTIMIZATION OF FIN STRUCTURE ON STAGGERED BATTERY PACK

According to the analysis as mentioned above, the increase in battery-fin contact thickness (X) shows different trends on $T_{\max}$ and ΔT. Specifically, the increase of A cannot alleviate the maximum battery temperature rise, but can improve temperature uniformity. Multiple combination solutions of battery-fin contact thickness (X) and fin width (A) make the uncertainty of the optimal solution increase. Therefore, it is essential to objectively assign weight coefficients to the evaluation indicators when choosing the optimal solution. In this section, $T_{\max}$ and ΔT are used as the evaluation indices for the comprehensive performance by the entropy weight-TOPSIS method to optimize the fin structure at 3C discharge rate. The specific analysis step is shown in Fig. 21.

5.1. Entropy weight-TOPSIS method

The entropy method is employed to discriminate between the degree of confusion in the given information, and information entropy is an evaluation tool that infers the utility value of the

indices among the inherent information on the basis of the entropy method. The smaller the information entropy of a given indicator, the greater the amount of effective information it provides, thus the more weight it carries in comprehensive evaluation. The entropy method is calculated according to the following steps:

i. Normalize the original matrix A:

$$A = \begin{bmatrix} a_{11} & a_{12} & \cdots & a_{1n} \\ a_{21} & a_{22} & \cdots & a_{2n} \\ \vdots & \vdots & \ddots & \vdots \\ a_{m1} & a_{m2} & \cdots & a_{mn} \end{bmatrix}, \quad (14)$$

where: m and n denote the number of evaluated solutions and indicators in the original information, respectively, a_{mn} represents the n-th evaluation indicator of the m-th solution.

For $T_{\max}$ and ΔT, the smaller the value, the better the thermal management efficiency of the battery module, thus it is necessary to perform positive and normalized processing before the calculation. The processed matrix is defined as B, the formula for which is determined by equation (15):

$$b_{ij} = \frac{\max_i \{a_{ij}\} - a_{ij}}{\max_i \{a_{ij}\} - \min_i \{a_{ij}\}}, \quad (15)$$

$$B = \begin{bmatrix} b_{11} & b_{12} & \cdots & b_{1n} \\ b_{21} & b_{22} & \cdots & b_{2n} \\ \vdots & \vdots & \ddots & \vdots \\ b_{m1} & b_{m2} & \cdots & b_{mn} \end{bmatrix}, \quad (16)$$
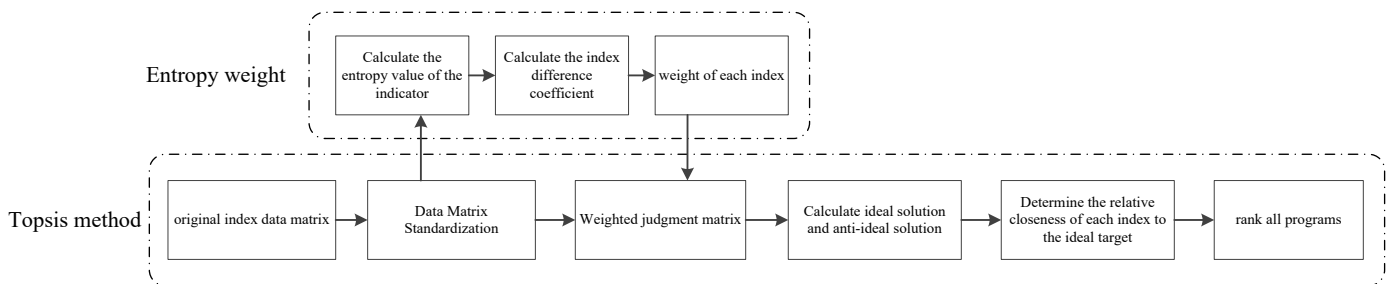

Fig. 21. Framework of entropy weight-TOPSIS method

where: $\max_i\{a_{ij}\}$ is the maximum value in the j-th evaluation index, and $\min_i\{a_{ij}\}$ denotes the minimum value of the j-th evaluation index.

ii. Calculation of the entropy value of the j-th evaluation index

$$e_j = -k\sum_i^m p_{ij}\ln p_{ij}, \quad 0 \le e_j \le 1, \tag{17}$$

where: k is a positive constant, whose expression is $1/\ln m$; p_{ij} is the weight of the i-th solution in the j-th evaluation index, as defined by equation (18):

$$p_{ij} = \frac{b_{ij}}{\sum_i^m b_{ij}}, 0 \le p_{ij} \le 1, \tag{18}$$

iii. Definition of the evaluation index information utility value

The entropy method assigns weight according to the dispersion degree for each index d_j, which can be calculated as:

$$d_j = 1 - e_j. \tag{19}$$

Therefore, the formula for calculating the weight coefficient of the j-th evaluation index w_j is:

$$w_j = \frac{d_j}{\sum_{j=1}^n d_j}. \tag{20}$$

The TOPSIS method is used to determine the optimal and inferior programs after obtaining various optimization target weights. Furthermore, the strengths and weaknesses of the assessment objects are weighed according to their proximity to the ideal solution before the optimal option is chosen. Specific calculation steps are as follows:

i. Construct weighted matrices Z_{ij} based on normalized matrix B:

$$Z_{ij} = (w_j b_{ij})_{m\times n}$$
$$= \begin{pmatrix} w_1 b_{11} & w_2 b_{12} & \cdots & w_n b_{1n} \\ \vdots & \vdots & & \vdots \\ w_m b_{m1} & w_2 b_{m2} & \cdots & w_m b_{mn} \end{pmatrix}. \tag{21}$$

ii. Determine the ideal solution z_{ij}^+ and anti-ideal solution z_{ij}^-:

$$\begin{cases} z_{ij}^+ = \max_{m,n}\left(z_1^+, z_2^+, \ldots, z_n^+\right), \\ z_{ij}^- = \min_{m,n}\left(z_1^-, z_2^-, \ldots, z_n^-\right). \end{cases} \tag{22}$$

iii. Calculate the distance between each solution to the z_{ij}^+ and the z_{ij}^-:

$$D_i^+ = \sqrt{\sum_{j=1}^n \left[z_{ij} - z_j^+\right]^2} \quad i = 1,2,\ldots m,$$
$$D_i^- = \sqrt{\sum_{j=1}^n \left[z_{ij} - z_j^-\right]^2} \quad i = 1,2,\ldots m. \tag{23}$$

iv. Calculate the relative proximity of each solution to the ideal solution C_i, and rank all programs based on this. A higher value of C_i indicates a superior option.

$$C_i = \frac{D_i^-}{D_j^+ + D_i^-}. \tag{24}$$

5.2. Optimization results of fin structure

The entropy weights of $T_{\max}$ and ΔT for the 625 group solutions are calculated using equation (14) to equation (20), and the results are shown in Table 6.

Table 6
Entropy weight results of evaluation indicators at 3C discharge rate

Index	Entropy value (e)	Index information utility value (d)	Entropy weight (w)
$T_{\max}$	0.9517	0.0483	54.44%
ΔT	0.9596	0.0404	45.56%

As shown in Table 6, the weight of $T_{\max}$ is higher than that of ΔT, indicating that $T_{\max}$ is equipped with a higher degree of dispersion than ΔT in the 625 groups, which has a greater impact on the comprehensive evaluation.

Based on the weights of each evaluation index, 625 groups of solutions with different structural parameters are further analyzed to explore the optimal structural parameters. Owing to space constraints, only the top 5 and bottom 5 solutions are presented in this paper, and the specific optimization results are shown in Table 7.

Table 7
Optimization results of battery pack structure parameters at 3C discharge rate

X [mm]	A [mm]	$T_{\max}$ [K]	ΔT [K]	D_i^+	D_i^-	C_i	RANK
0.67	0.60	312.30	0.10	0.039	0.671	0.946	1
0.83	0.60	312.42	0.05	0.047	0.67	0.935	2
0.83	0.60	312.40	0.09	0.048	0.663	0.932	3
0.67	0.60	312.30	0.14	0.049	0.663	0.931	4
0.50	0.60	312.24	0.17	0.053	0.666	0.926	5
3.83	0.55	315.06	1.17	0.652	0.060	0.084	621
3.83	0.54	315.02	1.19	0.651	0.059	0.084	622
4.00	0.53	315.05	1.17	0.652	0.059	0.083	623
4.00	0.53	315.03	1.18	0.651	0.059	0.083	624
3.83	0.54	315.04	1.18	0.651	0.059	0.083	625

As can be seen from Table 7, the distance between each evaluation solution and the optimal and inferior solutions can be accurately captured by the TOPSIS method at 3C discharge rate.

12

Bull. Pol. Acad. Sci. Tech. Sci., vol. 71, no. 4, p. e145677, 2023

The comprehensive thermal performance of the battery pack is relatively optimal when $X = 0.67$ mm and $A = 0.6$ mm, with a corresponding evaluation index of $T_{max} = 312.30$ K and $\Delta T = 0.10$ K, respectively, and a relative distance of 0.946 between the optimal solution and the ideal solution. When $X = 3.83$ mm and $A = 0.54$ mm, the battery pack shows the worst overall thermal performance, with the corresponding values of T_{max} and ΔT at 315.04 K and 1.18 K, while the relative closeness from this solution to the ideal solution is 0.083. According to the final optimization results, it can be concluded that the weight coefficients of T_{max} and ΔT greatly determine the optimal parameter structure. T_{max} possesses a higher weighting than ΔT, thus solutions with a lower maximum temperature are given priority in the ranking. Simultaneously, considering the weight of the temperature difference, the optimal solution is located among a total of 625 potential options.

6. CONCLUSIONS

A novel staggered PCM-fin thermal management system applied to lithium-ion battery storage is proposed in this study to solve the problem of battery storage with limited space and large energy density. The simulation focuses on the effect of fin structure dimensions, including battery-to-fin contact thickness (X) and fin width (A) on the heat dissipation performance of the battery pack. The entropy weight-TOPSIS method is introduced to search for the fin structure parameters with the optimal thermal management performance to meet the requirements of larger energy density and better heat dissipation efficiency. The following main conclusions are drawn from this study:

1. Based on the same fin structure within the limited volume of the aluminum container, the staggered battery pack with higher energy density reflects a higher value in T_{max} and ΔT, with 0.25 K and 1.39 K higher than the aligned arrangement, respectively. Both energy density and heat dissipation performance are considered, and the battery pack with staggered arrangement is preferred.

2. Due to the limitation of the battery pack size, the increase of X leads directly to the decrease in the effective utilization of PCM and the deterioration of maximum battery temperature. However, with the increase of contact area between fins and batteries, temperature uniformity within the battery pack is improved. Specifically, when the fin thickness (X) is changed from 0.5 mm to 4.5 mm, T_{max} increases by 1.71 K, 2.83 K, and 3.39 K, while ΔT decreases by 0.06 K, 0.42 K, and 0.72 K at 2C, 3C and 4C discharge rates, respectively.

3. The variation of fin width (A) has no significant effect on the thermal performance of the battery pack at different discharge rates. And the battery pack holds the best thermal performance when A is 0.5 mm. In detail, with the fin width (A) changing from 0.5 mm to 2.5 mm, T_{max} increases by 0.55 K, 0.97 K, 1.13 K, and ΔT increases by 0.11 K, 0.08 K and 0.08 K at 2C, 3C and 4C discharge rates, respectively.

4. The entropy weight-TOPSIS method is proposed to objectively evaluate 625 computational conditions of different fin parameter combination solutions, and T_{max} and ΔT are given weights of 54.44% and 45.56%, respectively. Based

on the weights obtained from the entropy weight method, the optimal fin structure parameters are found to be $X = 0.67$ mm and $A = 0.6$ mm, corresponding to T_{max} and ΔT of 315.04 K and 1.18 K, respectively.

REFERENCES

[1] R. Ma *et al.*, "Optimization of an Air-cooled battery pack with novel cooling channels based on silica cooling Plates," Appl. Therm. Eng., vol. 213, p. 118650, 2022, doi: 10.1016/j.applthermaleng.2022.118650.

[2] J. Cao, J. Feng, X.Fang, Z. Ling, and Z. Zhang, "A Delayed Cooling System Coupling Composite Phase Change Material and Nano Phase Change Material Emulsion," Appl. Therm. Eng., vol. 191, p. 116888, 2021, doi: 10.1016/j.applthermaleng.2021.116888.

[3] J. Weng, Y. He, D. Ouyang, X.Yang, G. Zhang, and J. Wang, "Thermal performance of PCM and Branch-structured fins for cylindrical power battery in a high-temperature Environment," Energy Conv. Manag., vol. 200, p. 112106, 2019, doi: 10.1016/j.enconman.2019.112106.

[4] D. Kong, R. Peng, P. Ping, J. Du, G. Chen, and J. Wen, "A novel battery thermal management system coupling with PCM and optimized controllable liquid cooling for different ambient Temperatures," Energy Conv. Manag., vol. 204, p. 112280, 2020, doi: 10.1016/j.enconman.2019.112280.

[5] X.Zhu, H. Shi, W. Xu, J. Pan, R. Zheng, and Y. Wang, "An improved air supply scheme for battery energy storage Systems," *Bull. Pol. Acad. Sci. Tech. Sci.*, vol. 70, no. 2, p. e140692, 2022, doi: 10.24425/bpasts.2022.140692.

[6] N. Wu, X.Ye, J. Li, B. Lin, X.Zhou, and B. Yu, "Passive Thermal Management Systems Employing Hydrogel for the Large-Format Lithium-Ion Cell: A Systematic Study," *Energy*, vol. 231, p. 120946, 2021, doi: 10.1016/j.energy.2021.120946.

[7] R. Zhou, J. Lu, X.Long, Y. Wu, L. Liu, and Y. Liu, "Theoretical model of lithium iron phosphate power battery under high-rate discharging for electromagnetic Launch," *Int. J. Mech. Sci.*, vol. 1, no. 2, pp. 220–229, 2021, doi: 10.1002/msd2.12014.

[8] H. Shi *et al.*, "Thermal Management Techniques for Lithium-Ion Batteries Based on Phase Change Materials: A Systematic Review and Prospective Recommendations," *Energies*, vol. 16, no. 2, p. 876, 2023, doi: 10.3390/en16020876.

[9] R. Kalbasi, "Introducing a novel heat sink comprising PCM and air – Adapted to electronic device thermal Management," *Int. J. Heat Mass Transfer*, vol. 169, p. 120914, 2021, doi: 10.1016/j.ijheatmasstransfer.2021.120914.

[10] H. Shi, M. Liu, W. Xu, X.Zhu, Y. Zou, and K. Yang, "Optimization on Thermal Management of Lithium-Ion Batteries Using Computational Fluid Dynamics and Air-cooling Methods," *Int. J. Electrochem. Sci.*, vol. 17, no. 5, p. 220550, 2022, doi: 10.20964/2022.05.46.

[11] Y. Xu, X.Li, X.Liu, Y. Wang, X.Wu, and D. Zhou, "Experiment investigation on a novel composite silica gel plate coupled with Liquid-cooling system for square battery thermal Management," *Appl. Therm. Eng.*, vol. 184, p. 116217, 2021, doi: 10.1016/j.appl thermaleng.2020.116217.

[12] X.Tang, Q. Guo, M. Li, C. Wei, Z. Pan, and Y. Wang, "Performance analysis on Liquid-cooled battery thermal management for electric vehicles based on machine Learning," *J. Power Sources*, vol. 494, p. 229727, 2021, doi: 10.1016/j.jpowsour.2021.229727.

Bull. Pol. Acad. Sci. Tech. Sci., vol. 71, no. 4, p. e145677, 2023

13

[13] W. Zhang, J. Qiu, X.Yin, and D. Wang, "A novel heat pipe assisted separation type battery thermal management system based on phase change Material," *Appl. Therm. Eng.*, vol. 165, p. 114571, 2020, doi: 10.1016/j.applthermaleng.2019.114571.

[14] N. Putra, A.F. Sandi, B. Ariantara, N. Abdullah, and T.M.I. Mahlia, "Performance of beeswax phase change material (PCM) and heat pipe as passive battery cooling system for electric Vehicles," *Case Stud. Therm. Eng.*, vol. 21, p. 100655, 2020, doi: 10.1016/j.csite.2020.100655.

[15] Y. Li *et al.*, "A novel Petal-type battery thermal management system with dual phase change Materials," *Int. J. Heat Mass Transf.*, vol. 207, p. 123989, 2023, doi: 10.1016/j.ijheatmasstransfer.2023.123989.

[16] X.Hu, C. Zhu, H. Wu, X.Li, X.Lu, and J. Qu, "Large-scale preparation of flexible phase change composites with synergistically enhanced thermally conductive network for efficient low-grade thermal energy recovery and Utilization," *Composites Part A*, vol. 154, p. 106770, 2022, doi: 10.1016/j.compositesa.2021.106770.

[17] P.R. Tete, M.M. Gupta, and S.S. Joshi, "Developments in battery thermal management systems for electric vehicles: A technical Review," *J. Energy Storage*, vol. 35, p. 102255, 2021, doi: 10.1016/j.est.2021.102255.

[18] D.K. Sharma and A. Prabhakar, "A review on air cooled and air centric hybrid thermal management techniques for Li-ion battery packs in electric Vehicles," *J. Energy Storage*, vol. 41, p. 102885, 2021, doi: 10.1016/j.est.2021.102885.

[19] N. Zheng, R. Fan, Z. Sun, and T. Zhou, "Thermal management performance of a fin-enhanced phase change material system for the lithium-ion Battery," *Int. J. Energy Res.*, vol. 44, no. 9, pp. 7617–7629, 2020, doi: 10.1002/er.5494.

[20] Tauseef-ur-Rehman, H.M. Ali, M.M. Janjua, U. Sajjad, and W. Yan, "A critical review on heat transfer augmentation of phase change materials embedded with porous materials/Foams," *Int. J. Heat Mass Transf.*, vol. 135, pp. 649–673, 2019, doi: 10.1016/j.ijheatmasstransfer.2019.02.001.

[21] R. Huang, Z. Li, W. Hong, Q. Wu, and X.Yu, "Experimental and numerical study of PCM thermophysical parameters on Lithium-ion battery thermal Management," *Energy Rep.*, vol. 6, pp. 8–19, 2020, doi: 10.1016/j.egyr.2019.09.060.

[22] J. Zhang *et al.*, "Characterization and experimental investigation of aluminum Nitride-based composite phase change materials for battery thermal Management," *Energy Convers. Manage.*, vol. 204, p. 112319, 2020, doi: 10.1016/j.enconman.2019.112319.

[23] H. Nazir *et al.*, "Recent developments in phase change materials for energy storage applications: A Review," *Int. J. Heat Mass Transf.*, vol. 129, pp. 491–523, 2019, doi: 10.1016/j.ijheatmasstransfer.2018.09.126.

[24] R. Fan, N. Zheng, and Z. Sun, "Evaluation of fin intensified phase change material systems for thermal management of Li-ion battery Packs," *Int. J. Heat Mass Transf.*, vol. 166, p. 120753, 2021, doi: 10.1016/j.ijheatmasstransfer.2020.120753.

[25] A. Verma and D. Rakshit, "Performance analysis of PCM-fin combination for heat abatement of Li-ion battery pack in electric vehicles at high ambient Temperature," *Therm. Sci. Eng. Prog.*, vol. 32, p. 101314, 2022, doi: 10.1016/j.tsep.2022.101314.

[26] S. Ambekar, P. Rath, and A. Bhattacharya, "A novel PCM and TCE based thermal management of battery Pack," *Therm. Sci. Eng. Prog.*, vol. 29, p. 101196, 2022, doi: 10.1016/j.tsep.2022.101196.

[27] X.Qi *et al.*, "Optimization and Sensitivity Analysis of Extended Surfaces during Melting and Freezing of Phase Changing Materials in Cylindrical Lithium-Ion Battery Cooling," *J. Energy Storage*, vol. 51, p. 104545, 2022, doi: 10.1016/j.est.2022.104545.

[28] I.B. Mansir, N. Sinaga, N. Farouk, M. Aljaghtham, C. Diyoke, and D. Nguyen, "Numerical simulation of dimensions and arrangement of triangular fins mounted on cylindrical Lithium-ion batteries in passive thermal Management," *J. Energy Storage*, vol. 50, p. 104392, 2022, doi: 10.1016/j.est.2022.104392.

[29] R. Akula and C. Balaji, "Thermal management of 18650 Li-ion battery using novel fins–PCM–EG composite heat Sinks," *Appl. Energy*, vol. 316, p. 119048, 2022, doi: 10.1016/j.apenergy.2022.119048.

[30] V.G. Choudhari, A.S. Dhoble, and S. Panchal, "Numerical analysis of different fin structures in phase change material module for battery thermal management system and its Optimization," *Int. J. Heat Mass Transf.*, vol. 163, p. 120434, 2020, doi: 10.1016/j.ijheatmasstransfer.2020.120434.

[31] Z. Chen, X.Li, J. Zhang, and L. Ouyang, "Simulation and analysis of heat dissipation performance of power battery based on phase change material enhanced heat transfer variable fin Structure," *Numer. Heat Transfer, Part A*, vol. 80, no. 11, pp. 535–555, 2021, doi: 10.1080/10407782.2021.1959834.

[32] D. Bernardi, E. Pawlikowski, and J. Newman. "A General Energy Balance for Battery Systems," *J. Electrochem. Soc.*, vol. 132, no. 1, pp. 5–12, 1985, doi: 10.10.1149/1.2113792.

[33] J. Liu, F. Tavakoli, S.M. Sajadi, M.Z. Mahmoud, B. Heidarshenas, and H.Ş. Aybar, "Numerical evaluation and artificial neural network modeling of the effect of oval PCM compartment dimensions around a triple Lithium-ion battery pack despite forced Airflow," *Eng. Anal. Bound. Elem.*, vol. 142, pp. 71–92, 2022, doi: 10.1016/j.enganabound.2022.05.006.

[34] M. Fadl, and P. Eames, "A Numerical Investigation into the Heat Transfer and Melting Process of Lauric Acid in a Rectangular Enclosure with Three Values of Wall Heat Flux," *Energy Procedia*, vol. 158, pp. 4502–4509, 2019, doi: 10.1016/j.egypro.2019.01.761.